



HAL
open science

Sequence optimization for high frame rate imaging with a convex array

Nina Ghigo, Alessandro Ramalli, Stefano Ricci, Piero Tortoli, Didier Vray,
Herve Liebgott

► **To cite this version:**

Nina Ghigo, Alessandro Ramalli, Stefano Ricci, Piero Tortoli, Didier Vray, et al.. Sequence optimization for high frame rate imaging with a convex array. IEEE International Ultrasonics Symposium, Sep 2020, Las Vegas, United States. hal-03024787

HAL Id: hal-03024787

<https://hal.science/hal-03024787>

Submitted on 26 Nov 2020

HAL is a multi-disciplinary open access archive for the deposit and dissemination of scientific research documents, whether they are published or not. The documents may come from teaching and research institutions in France or abroad, or from public or private research centers.

L'archive ouverte pluridisciplinaire **HAL**, est destinée au dépôt et à la diffusion de documents scientifiques de niveau recherche, publiés ou non, émanant des établissements d'enseignement et de recherche français ou étrangers, des laboratoires publics ou privés.

Sequence optimization for high frame rate imaging with a convex array

Nina Ghigo¹, Alessandro Ramalli², Stefano Ricci², Piero Tortoli², Didier Vray¹, Hervé Liebgott¹

¹Univ. Lyon, INSA-Lyon, UCBL, UJM-Saint-Etienne, CNRS, Inserm, CREATIS UMR 5220, U1206, F-69621 Lyon, France

²Department of Information Engineering, University of Florence, 50139 Florence, Italy

nina.ghigo@creatis.insa-lyon.fr

Abstract— In this paper, five different sequences for image compounding at a high frame rate with very few sub-images are investigated for abdominal exploration with a convex probe. Simulation and experiments using a ULA-OP 256 scanner were made to compare the resolution and contrast-to-noise ratio (CNR) of the different sequences. The best configuration is based on a sliding apodization window, gives a resolution of 1° (i.e. 2.1 mm) and CNR of 12.4 dB at 6 cm depth in a Gammex Sono403™ phantom. A frame rate of 1.2 kHz can be achieved at 20 cm depth. This high-frame rate sequence has been chosen to allow the study of fast transient phenomena such as the pulse wave propagation and peak systolic velocity in deep vessels like the abdominal aorta.

Keywords—high-frame rate, compounding, virtual source, convex array

I. INTRODUCTION

Over the past two decades, new ultrasound imaging sequences referred to as high frame rate imaging have been developed. Depending on the depth of investigation, a frame rate higher than 10 kHz can be obtained using plane or diverging waves. However, if only one wave is used, this increase in frame rate comes at the price of image quality in terms of resolution and contrast. To overcome this issue, compounding techniques [1] have been developed, allowing to recover an image quality comparable to conventional focused transmissions. Several plane or diverging waves are transmitted successively in the medium with different incident angles generating backscattered echoes containing different information. By coherently combining sub-images obtained through the beamforming of the backscattered signals of each emission, a synthetic transmit focusing is achieved, which improves image quality. One drawback of compounding methods is that the final frame rate is divided by the number of sub-images to be compounded: a compromise must be reached between frame rate increase and image quality.

Optimal compounding sequences have been extensively studied for linear or phased arrays probes [2], [3]. Way less work has been carried out for convex probes. Jensen et al [4] have proposed a compounding sequence using synthetic aperture leading to a frame rate independent of the number of emissions with a convex probe. However, the rather complex computation for synthetic aperture imaging heavily affects the post-processing.

The context of this work is the development of high frame rate imaging modes for deep vessels exploration in the abdomen. In clinical practice, convex probes are used to image the abdominal cavity, as they have a larger field of view and their frequency is typically lower, allowing a deeper tissue exploration, compared to linear probes. The study of fast

phenomena in arteries, such as pulse wave propagation, high flow velocity at the systolic peak and vortex formation, has already shown its clinical value for both diagnosis, prevention, and understanding of cardiovascular diseases [5], [6]. Most of the previous work focused on the carotid artery, a shallow vessel (<3cm deep) with easy access using a linear probe, and are not directly implementable to a convex probe [7], [8]. Furthermore, the phenomena occurring in the abdominal aorta (AA) tend to be faster than those in the carotid artery. As the abdominal aorta is deeper than the carotid, the round-trip time of the ultrasound wave greatly limits the achievable frame rate. In this paper, our goal is to achieve a compounded imaging sequence allowing the study of fast phenomena while considering the limitation set by a large imaging depth.

In the following section, the clinical context of this study will be detailed. Section III presents the different compounding sequences investigated as well as the simulation and experiments carried out. The results of both simulation and experiments are presented in Section IV. Finally, Sections V and VI conclude the paper with a discussion of the results and a conclusion.

II. CLINICAL CONTEXT AND LIMITATION

The abdominal aorta (AA) is located under the abdominal fat and its depth can greatly vary from 5 to 20 cm. Its normal healthy diameter is around 2 cm. As the study of vascular diseases becomes more relevant with age and when the patient tends to be fatter, we consider the worst case condition i.e. AA being at 20 cm depth. The round-trip time of the ultrasound wave leads to a limitation of the pulse repetition frequency given by:

$$PRF_{max} = \frac{c}{2 r_{AA}} \quad 1)$$

where c is the speed of sound in the medium and r_{AA} is the radial distance between the probe and the center of the AA. If we take c equal to 1540 m/s and r_{AA} equals 21 cm, we obtain a maximum PRF of 3.7 kHz.

The phenomena occurring in the AA are fast and transient. The peak systolic velocity is typically around 120 cm/s while the pulse wave velocity is around 5 m/s. Typically, flow velocity is measured by Doppler techniques, over a range limited by the Nyquist velocity:

$$v_{max} = \frac{PRF \lambda}{4} \quad 2)$$

We can hence find the minimum PRF to be able to observe such fast phenomena:

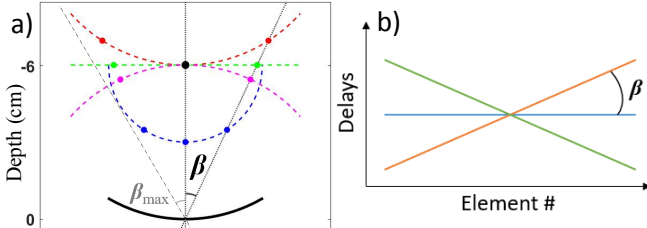


Figure 2: The different configurations are represented (blue: cfg haR, red: cfg rad, green: cfg hoL, pink: cfg anR). β is the angle setting the spacing between VSs and the black line represents the probe surface. b) representation of the different linear delays for cfg DWs.

TABLE I PROBE PARAMETERS

Number of elements	192
Radius of curvature	$R = 60.3$ mm
Field of view	$-30^\circ/30^\circ$

$$PRF_{min} = \frac{4 v_{max}}{\lambda} \quad 3)$$

A typical convex probe has a center frequency f_c around 3 MHz, leading to a wavelength λ of $c/f_c \approx 0.5$ mm. If we want to observe the peak systolic velocity of the AA, we obtain a PRF_{min} of 1 kHz.

With these constraints on the PRF , we can deduce that only 3 emissions can be compounded. To the best of our knowledge, no previous work has studied the compounding sequence of a convex probe with such stringent constraints.

III. MATERIALS AND METHODS

A. Compounding sequences

In this work, five different configurations (cfg) of virtual sources (VS) spatial distributions were investigated through simulations and experiments. The CA631 convex probe (Esaote, Italy), whose parameters are given in TABLE I, was used. VS were evenly distributed on either the half-radius (haR), the radius (rad), a horizontal line through the array pivot (hoL), or the anti-radius (anR) as represented in Figure 1 a). The three VS positions were calculated with their corresponding angles $(-\beta, 0, \beta)$. Different value for β , ranging from 5 to 40° in 5° steps, were tested. For cfg haR and rad, the maximum possible β_{max} value is 30°, as illustrated in Figure 1. Finally, diverging waves (DWs) achieved by linear delays with a steering angle $= \beta$ were also tested (Figure 1 b)). The apodizations in emission and reception were given by a Hanning window over all elements of the probe, except for the haR cfg where a sliding Hanning window of 128 elements is used in emission. These configurations are compared to a single diverging wave following the array curvature (1DW) i.e. with no delays.

B. Image formation

Each position of VS defined a different delay in emission. The backscattered echoes are beamformed with a delay-and-sum (DAS) algorithm. In this paper, we have studied the directivity of the elements to select only relevant data during the DAS summation [12].

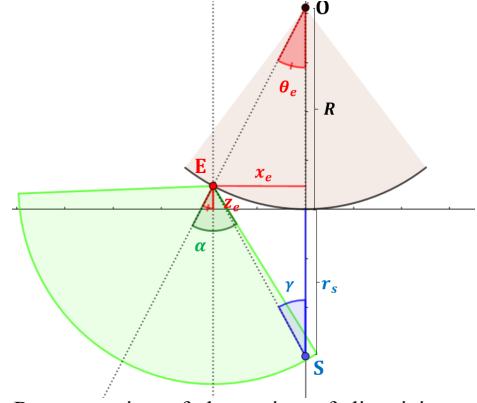


Figure 1: Representation of the notion of directivity α with a convex probe of center O and radius R . E is an element of the probe and S a scatterer.

TABLE II ACQUISITION PARAMETERS

Transmit frequency	$f_c = 3.5$ MHz
Sampling frequency	12.5 MHz in simulation 39 MHz in experiments
Transmit burst	3-cycle sinusoidal burst
Speed of sound	$c = 1540$ m/s
Pulse repetition frequency	$PRF = 3000$ Hz
Transmit apodization	Hanning on all elements Sliding Hanning on 128 elements for cfg haR
Receive apodization	Hanning on all elements
Number of scatterers per mm ² for simulation	$\frac{1}{\lambda} \approx 2000$

The directivity of an element of width w , depends on the insonification angle ϑ . For a piston-like element in a soft baffle (doc), which is a current assumption, it is given by [12]:

$$D(\vartheta) = \cos(\vartheta) \operatorname{sinc}\left(\pi \frac{w}{\lambda} \sin(\vartheta)\right) \quad 4)$$

where λ is the wavelength propagating in the medium, in our case $\lambda \approx 0.5$ mm. Heuristically we consider the backscattered echoes only if $D(\vartheta) > 3$ dB, leading to a directivity α of approximately 27° in our case.

In Figure 2, we represent the convex probe of center O and radius R . An element E is displayed with its polar (R, θ_e) and its cartesian (x_e, z_e) coordinates. Its directivity at -3dB is represented by the green cone of angle α . For schematic purpose α is here way bigger than typical directivity. For calculus purpose, the angle γ is defined between a scatterer S located on z -axis and the element E . The backscattered echoes from S need to be considered only if they are visible by the element E i.e. only if:

$$|\alpha - \theta_e| > \gamma \quad 5)$$

We can compute γ :

$$\gamma = \tan^{-1}\left(\frac{x_e}{r_s + R - z_e}\right) \quad 6)$$

It is easily possible to go from cartesian to polar coordinates through:

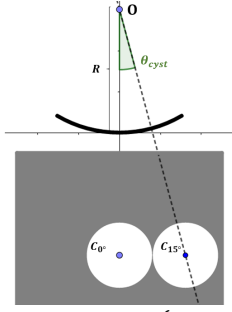


Figure 3: The scatterers (a) and the anechoic cysts (b) positions used in simulation are sketched.

$$\begin{cases} x_e = R \sin(\theta_e) \\ z_e = R \cos(\theta_e) \end{cases} \quad (7)$$

Equation 6) then becomes:

$$\gamma = \tan^{-1} \left(\frac{\sin(\theta_e)}{r_s/R + 1 - \cos(\theta_e)} \right) \quad (8)$$

As $|\alpha - \theta_e|$ is known for each element of the probe, it is possible to determine for every point of interest in the medium if it should be considered or not.

C. Data acquisition

Simulations were performed through SIMUS [13] on two 6 cm deep anechoic cysts aligned C_{0° and angled at 15° C_{15° with the probe (Figure 3).

Experiments were performed using a ULA-OP 256 scanner [14] and a CA631 Esaote convex probe on the Gammex Sono403™ phantom. We focus our attention on the scatterer and the anechoic cyst located at 6 cm (Figure 4). Simulation and experiment parameters are shown in Table II.

D. Performance measures

The resolution, measured as the width of the PSF at -6 dB, is computed on the data in polar coordinates, which leads to a resolution in radian or degree. This is done to evaluate the resolution in the correct direction of the PSF. The following equation is used to convert the resolution in radian $reso_{rad}$ to

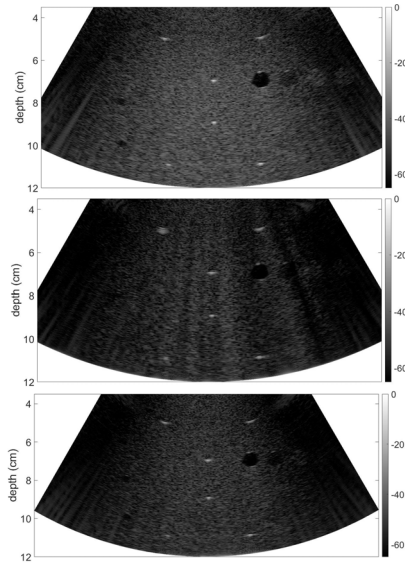


Figure 4: The best (a) and the worst (b) B-mode images of the Gammex phantom in terms of contrast and resolution are displayed in dB. c) shows the image 1DW (without compounding)

meter $reso_m$ knowing the radial distance r_s where the resolution was computed:

$$reso_m = reso_{rad}(R + r_s) \quad (9)$$

Similarly, the contrast to noise ratio (CNR) is computed on the final compounded image B-mode in polar coordinates to avoid the influence of interpolation.

$$CNR = 20 \log_{10} \left(\frac{|\mu_{cyst} - \mu_{bg}|}{\sqrt{\sigma_{cyst}^2 + \sigma_{bg}^2/2}} \right) \quad (10)$$

where μ_{cyst} and μ_{bg} (σ_{cyst}^2 and σ_{bg}^2) are the means (variances) pixel values, after log compression, of the cyst and the background regions, respectively.

IV. RESULTS

The CNR values obtained on the compounded final image in simulation and experimentation are reported in Figure 5.

A. Simulation

In simulation, the CNR obtained on the centered and angled cysts vary quite irregularly with the cfg and β angle. The maximum difference in terms of contrast is less than 1 dB, which is quite low. With only the simulated data it is impossible to conclude on the best cfg. The CNR obtained on the centered and angle cysts with only one diverging wave (1DW) is 12.6 and 10.8 dB, respectively.

B. Gammex experimentation

In terms of resolution, cfg DWs gives poor results, showing the great difference between the use of a linear and convex probe. cfg rad, hoL and anR give pretty similar results, which is coherent as their VS are near to each other. The best β angle for these cfg is 15° , where the resolution is less than 1.1° i.e. 2.3 mm thanks to 9). The cfg giving the best resolution is haR where its minimum resolution of 0.95° (2 mm) is obtained at $\beta = 25^\circ$.

The cfg behave similarly for the CNR, where cfg DWs gives the poorest results, cfg rad, hoL and anR have similar behavior with a best CNR higher than 12 dB at $\beta = 5^\circ$. For cfg haR, the best CNR of 12.4 dB for $\beta = 20^\circ$.

For the cfg haR (the best one), if we both consider resolution and CNR, the best angles are $\beta = 25^\circ$ and $\beta = 20^\circ$ respectively. For $\beta = 25^\circ$, the CNR decreased rather heavily at 11.15 dB. For $\beta = 20^\circ$, the resolution increased by less than 0.05° leading to a resolution of 1° (2.1 mm).

The best compromise between resolution and CNR seems then to be the sliding cfg haR at $\beta = 20^\circ$ displayed in Figure 4. For comparison purposes, the worst-case image (cfg DWs; $\beta=5^\circ$) alongside with 1DW (no compounding) are also displayed.

The CNR and resolution obtained with only one diverging wave (1DW) is respectively 9.1 dB and 1° .

V. DISCUSSION

The best configuration in terms of image quality in both resolution and contrast-to-noise ratio has been investigated. Other performance measures could have been used, such as speckle size measurement [4].

The reason for the discrepancy we observe on the CNR obtained in simulation versus the experiments remains unknown and will be the subject of further investigations.

For a linear array, one of the most used sequences is angled linear delays, done in cfg DWs. For a convex probe, cfg DWs gives the poorest results highlighting the need of specific compounding sequences for convex probes. As shown in III.B, only relevant data should be considered during image formation. This may explain why the best configuration is the one with a sliding window apodization that does not consider all elements (cfg haR). Similarly, sending one diverging wave in the medium (cfg 1DW) can give a better image quality than a poor compounding sequence.

VI. CONCLUSION

In this paper, a configuration of three virtual sources was presented for high-frame rate compounding. The goal of future work will be to use this sequence in an abdominal aorta phantom to estimate simultaneously the motion of the blood flow and the wall.

REFERENCES

- [1] G. Montaldo, M. Tanter, J. Bercoff, N. Benech, and M. Fink, "Coherent plane-wave compounding for very high frame rate ultrasonography and transient elastography," *IEEE Trans. Ultrason. Ferroelectr. Freq. Control*, vol. 56, no. 3, pp. 489–506, 2009, 10.1109/TUFFC.2009.1067.
- [2] O. Couture, M. Fink, and M. Tanter, "Ultrasound contrast plane wave imaging," *IEEE Trans. Ultrason. Ferroelectr. Freq. Control*, vol. 59, no. 12, p. 6373790, 2012, 10.1109/TUFFC.2012.2508.
- [3] J. Poree, D. Posada, A. Hodzic, F. Tournoux, G. Cloutier, and D. Garcia, "High-Frame-Rate Echocardiography Using Coherent Compounding With Doppler-Based Motion-Compensation," *IEEE Trans. Med. Imaging*, vol. 35, no. 7, pp. 1647–1657, 2016, 10.1109/TMI.2016.2523346.
- [4] J. M. Hansen and J. A. Jensen, "Performance of synthetic aperture compounding for in-vivo imaging," in *2011 IEEE IUS*, Orlando, FL, USA, 2011, pp. 1148–1151, 10.1109/ULTSYM.2011.0282.
- [5] A. Kheradvar and G. Pedrizzetti, "Vortex Formation in the Heart," in *Vortex Formation in the Cardiovascular System*, London: Springer London, 2012, pp. 45–79.
- [6] K. Fujikura *et al.*, "A Novel Noninvasive Technique for Pulse-Wave Imaging and Characterization of Clinically-Significant Vascular Mechanical Properties *In Vivo*," *Ultrason. Imaging*, vol. 29, no. 3, pp. 137–154, 2007, 10.1177/016173460702900301.
- [7] J. Udesen, F. Gran, K. Hansen, J. A. Jensen, C. Thomsen, and M. B. Nielsen, "High frame-rate blood vector velocity imaging using plane waves: Simulations and preliminary experiments," *IEEE Trans. Ultrason. Ferroelectr. Freq. Control*, vol. 55, no. 8, pp. 1729–1743, 2008, 10.1109/TUFFC.2008.858.
- [8] V. Perrot, H. Liebgott, A. Long, and D. Vray, "Simultaneous tissue and flow estimation at high frame rate using plane wave and transverse oscillation on in vivo carotid," presented at the 2018 IEEE International Ultrasonics Symposium (IUS), 2018, 10.1109/ULTSYM.2018.8580182.
- [9] M. Couade *et al.*, "Ultrafast imaging of the arterial pulse wave," *IRBM*, vol. 32, no. 2, pp. 106–108, 2011, 10.1016/j.irbm.2011.01.012.
- [10] A. Dogui *et al.*, "Consistency of aortic distensibility and pulse wave velocity estimates with respect to the Bramwell-Hill theoretical model: a cardiovascular magnetic resonance study," *J. Cardiovasc. Magn. Reson.*, vol. 13, no. 1, p. 11, 2011, 10.1186/1532-429X-13-11.
- [11] P. Scheel, C. Ruge, and M. Schöning, "Flow velocity and flow volume measurements in the extracranial carotid and vertebral arteries in healthy adults: reference data and the effects of age," *Ultrasound Med. Biol.*, vol. 26, no. 8, pp. 1261–1266, 2000, 10.1016/S0301-5629(00)00293-3.
- [12] A. R. Selfridge, G. S. Kino, and B. T. Khuri-Yakub, "A theory for the radiation pattern of a narrow strip acoustic transducer," *Appl. Phys. Lett.*, vol. 37, no. 1, pp. 35–36, 1980, 10.1063/1.91692.
- [13] S. Shahriari and D. Garcia, "Meshfree simulations of ultrasound vector flow imaging using smoothed particle hydrodynamics," *Phys. Med. Biol.*, vol. 63, no. 20, p. 205011, 2018, 10.1088/1361-6560/aae3c3.
- [14] E. Boni *et al.*, "ULA-OP 256: A 256-Channel Open Scanner for Development and Real-Time Implementation of New Ultrasound Methods," *IEEE Trans. Ultrason. Ferroelectr. Freq. Control*, vol. 63, no. 10, pp. 1488–1495, 2016, 10.1109/TUFFC.2016.2566920.

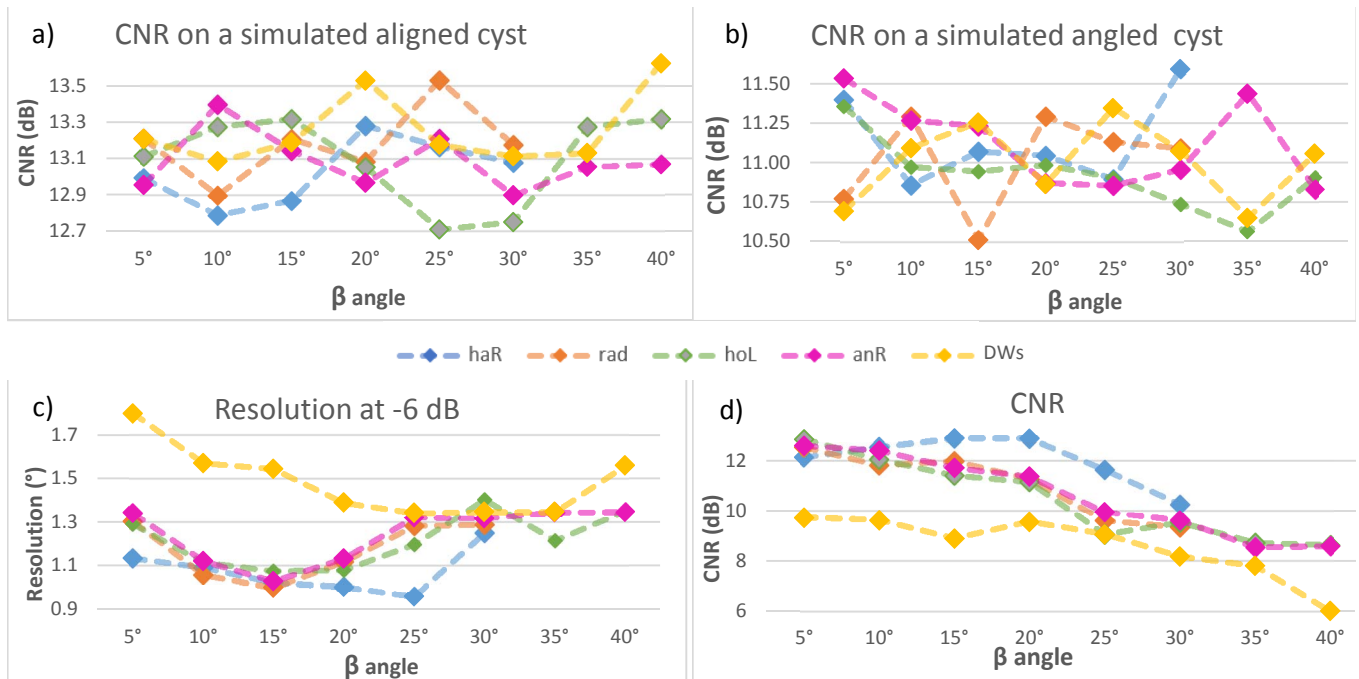


Figure 5: The CNR obtained on the simulated anechoic cysts are showed in a) and b). The resolution in degree, and CNR, obtained on the 6 cm-deep scatterer of the Gammex phantom are showed in b) and c).